

Ionization-Facilitated Formation of 2D (Alumino)Silicate–Noble Gas Clathrate Compounds

Jian-Qiang Zhong, Mengen Wang, Nusnin Akter, John D. Kestell, Tianchao Niu, Alejandro M. Boscoboinik, Taejin Kim, Dario J. Stacchiola, Qin Wu, Deyu Lu,* and Jorge Anibal Boscoboinik*

The nanoscale confinement of noble gases at noncryogenic temperatures is crucial for many applications including noble gas separations, nuclear waste remediation, and the removal of radon. However, this process is extremely difficult primarily due to the weak trapping forces of the host matrices upon noble gas physisorption. Herein, the formation of 2D clathrate compounds, which result from trapping noble gas atoms (Ar, Kr, and Xe) inside nanocages of ultrathin silica and aluminosilicate crystalline nanoporous frameworks at 300 K, is reported. The formation of the 2D clathrate compounds is attributed to a novel activated physisorption mechanism, facilitated by ionization of noble gas atoms. Combined X-ray photoelectron spectroscopy (XPS) and density functional theory (DFT) studies provide evidence of an initial ionization process that significantly reduces the apparent trapping barrier. Noble gas ions become neutralized upon entering the cages, and their desorption requires unprecedentedly high temperatures, even in ultrahigh vacuum conditions. From 2D aluminosilicate films these temperatures are 348 K (Ar), 498 K (Kr), and 673 K (Xe). DFT calculations also predict that Rn can be trapped in 2D aluminosilicates with an even higher desorption temperature of 775 K. This work highlights a new ionization-facilitated trapping mechanism resulting in the thinnest family of clathrates ever reported.

1. Introduction

Noble gases (elements in the group 18) are the most unreactive elements in the periodic table. Their condensation temperatures are 4 K (He), 27 K (Ne), 87 K (Ar), 120 K (Kr), 165 K (Xe), and 211 K (Rn). Consequently, immobilizing them on a surface normally requires very low temperatures. Trapping them at noncryogenic conditions is an industrially relevant challenge for energy, environment, and health applications.^[1] For example, radioactive isotopes of Kr and Xe are a byproduct of nuclear fission in nuclear plants and, due to their volatile nature, their release to the atmosphere is hard to control.^[2] Rn is radioactive and a known carcinogen, responsible for 15% of lung cancers worldwide.^[3] Intensive research efforts have been devoted to the fundamental understanding of intrinsic physical and chemical properties of isolated noble gas atoms in confinement.^[4] Electrostatic trapping of Xe has been reported by using

a boron nitride nanomesh formed on Rh(111), but it is still at cryogenic temperatures.^[5] Ion implantation is the only method that has been explored at room temperature to trap noble gas atoms under a 2D graphene cover by ionizing the atoms and accelerating them toward the surface under an applied electrostatic potential.^[6] However, the substantial surface defects induced by ion implantation also result in uncontrolled noble gas “blisters.”


From the point of view of surface science, the adsorption of a molecule on a surface can be either physisorption or chemisorption^[7] as illustrated in Figure 1A. While the former exhibits a small adsorption energy ($|\Delta E_{\text{ads}}|$) at the potential energy minimum due to weak van der Waals (vdW) interactions, the latter binds a molecule tightly through chemical bonds with a much larger $|\Delta E_{\text{ads}}|$. Since noble gas atoms are extremely difficult to form strong chemical bonds with the surface, the fundamental challenge of trapping noble gases at noncryogenic conditions mainly originates from the small $|\Delta E_{\text{ads}}|$ in physisorption.^[8] Here we report an activated physisorption mechanism that traps noble gas atoms with an ultrahigh desorption energy barrier (E_{des}) as shown in Figure 1A. This trapping process

Dr. J.-Q. Zhong, M. Wang, N. Akter, Dr. J. D. Kestell, Dr. T. Niu, Dr. D. J. Stacchiola, Dr. Q. Wu, Dr. D. Lu, Dr. J. A. Boscoboinik
Center for Functional Nanomaterials
Brookhaven National Laboratory
Upton, NY 11973, USA
E-mail: dlu@bnl.gov; jboscoboinik@bnl.gov

M. Wang, N. Akter, Prof. T. Kim
Materials Science and Chemical Engineering Department
Stony Brook University
Stony Brook, NY 11790, USA

A. M. Boscoboinik
Instituto de Física Aplicada INFAP
CONICET
Departamento de Física
Universidad Nacional de San Luis
Chacabuco, 917-5700 San Luis, Argentina

A. M. Boscoboinik
Department of Chemistry
University of Wisconsin-Milwaukee
Milwaukee, WI 53211, USA

 The ORCID identification number(s) for the author(s) of this article can be found under <https://doi.org/10.1002/adfm.201806583>.

DOI: 10.1002/adfm.201806583

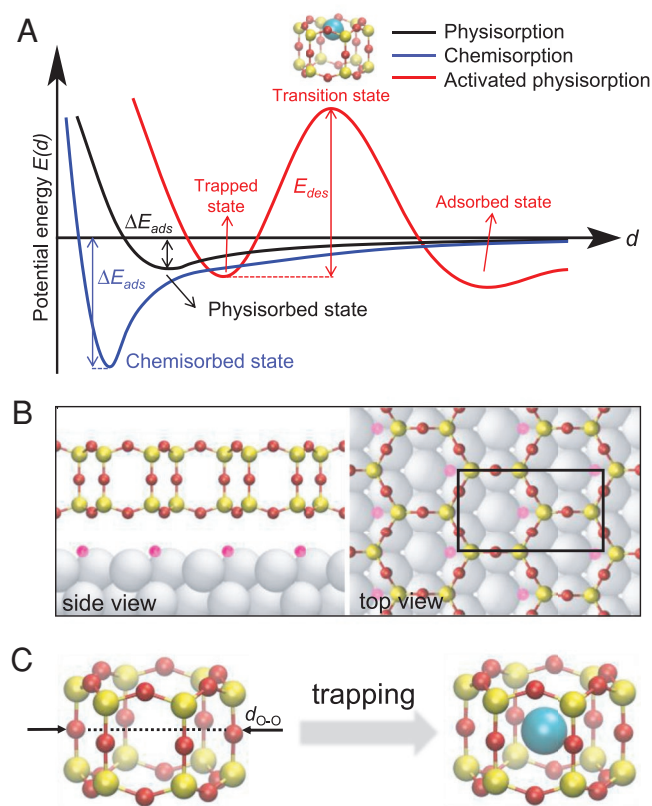


Figure 1. Potential energy diagram and structure of the 2D silica. A) Schematic diagram of the potential energies against the distance from contact surface (d) for physisorption, chemisorption, and activated physisorption, respectively. ΔE_{ads} represents the adsorption energy; E_{des} represents the desorption energy barrier for activated physisorption. B) Side (left) and top (right) views of the 2D silica bilayer film adsorbed on $p(2 \times 1)\text{-O/Ru(0001)}$ (i.e., $(\text{SiO}_2)_8/4\text{O/Ru(0001)}$). The black rectangle on the top view indicates the unit cell. C) Illustrations of the nanocages in the framework with and without the noble gas atom trapped inside. Color code: Ru (silver), Si (yellow), O in silica (red), and O chemisorbed on Ru (pink).

forms 2D clathrate compounds, where noble gases are immobilized in the nanocages of the host 2D (alumino)silicate.

2D (alumino)silicate (silica: SiO_2 and aluminosilicate: $\text{Al}_x\text{Si}_{1-x}\text{O}_2$) are recently reported ultrathin nanoporous crystalline frameworks.^[9] Their structures are shown in Figure 1B. These frameworks have been proposed as model systems for surface science studies of zeolites,^[9b,10] which are the most widely used catalysts in the industry^[11] and the most important sorbent materials.^[12] The well-ordered 2D (alumino)silicate frameworks with a thickness less than 5 Å were grown on a Ru(0001) surface, in which the distance between the (alumino)silicate framework and the ruthenium surface ranges between 2 and 4 Å depending on the coverage of interfacial chemisorbed oxygen.^[13] Other supports have also been reported, including Pt(111), Pd(111), Pd(100), and $\text{Ni}_x\text{Pd}_{1-x}$ (111) alloys.^[14] The building unit of such a bilayer framework is the hexagonal prism nanocage shown in Figure 1C. Interestingly, high solubility of noble gases was recently reported for a naturally occurring (alumino)silicate mineral that also contains

hexagonal rings,^[15] in the context of rationalizing the higher-than-expected concentration of noble gases in the earth mantle.

We recently reported that 2D (alumino)silicate films are able to trap single Ar atoms, where both desorption measurements and density functional theory (DFT) calculations point to a high desorption barrier of about 1 eV.^[16] However, these results created a big puzzle, namely, if the activation energy barrier for Ar to enter these nanocages is at a similar magnitude (≈ 1 eV), how did Ar atoms get trapped inside nanocages at room temperature below the atmosphere pressure? Based on DFT calculations, Yao et al. claimed that the energy barrier is too high for Ar to go through the nanopores in the 2D silica films.^[17] In this study, we investigated the trapping mechanism in detail and confirmed that noble gas trapping by 2D (alumino)silicate films is an activated physisorption process. The seemingly contradicting conclusions of our study and ref. [17] can be reconciled by a strong ionization-induced trapping/desorption activation barrier parity, which means that noble gas atoms enter the nanocages in the form of ions with a significantly reduced trapping energy barrier and exit as neutral atoms with an ultrahigh desorption energy barrier. We further extended this study to all noble gases except the newly discovered Og, which has a very short lifetime, and found that these 2D (alumino)silicate films can trap individual atoms of Ar, Kr, and Xe with unprecedentedly high kinetic stability, while He and Ne are too small to remain in the nanocage. DFT calculations predict the trapping of Rn. Unlike ion implantation, our approach is non-destructive as the trapping process does not create defects on the 2D (alumino)silicate, which makes the trapping and release processes reversible. We further demonstrated that the notable differences in thermal stabilities of noble gases can be exploited to separate a mixture of Ar, Kr, and Xe.

2. Results and Discussion

2.1. Noble Gas Trapping

Trapping noble gas atoms in (alumino)silicate nanocages is demonstrated in situ by X-ray photoelectron spectroscopy (XPS). A silica bilayer was separately exposed to low pressures (≈ 2 mbar) of individual noble gases (He, Ne, Ar, Kr, and Xe) at room temperature. Simultaneously acquired ambient pressure XPS (AP-XPS) spectra show strong gas phase core level peaks (Figure S1, Supporting Information). As the gas pressure is lowered, these gas phase peaks decrease and eventually disappear, while newly evident peaks located at the lower binding energy (E_{BE}) side remain over time even after evacuating the experimental chamber in the cases of Ar, Kr, and Xe, as shown in Figure S1 (Supporting Information). These peaks are assigned to trapped noble gas atoms in the silica bilayer/Ru(0001) system. Consistent with our previous results,^[16] while most trapped atoms are located in the cages, there is a small fraction of noble gas atoms located as well at the interface between the silica/Ru(0001) interface. This minority species is evident in the deconvolution of the Ar 2p, Kr 3d, and Xe 3d_{5/2} core level spectra shown in Figure S2 (Supporting Information) as a small component on the lower binding energy side. The peak assignment is in agreement with DFT calculations, from

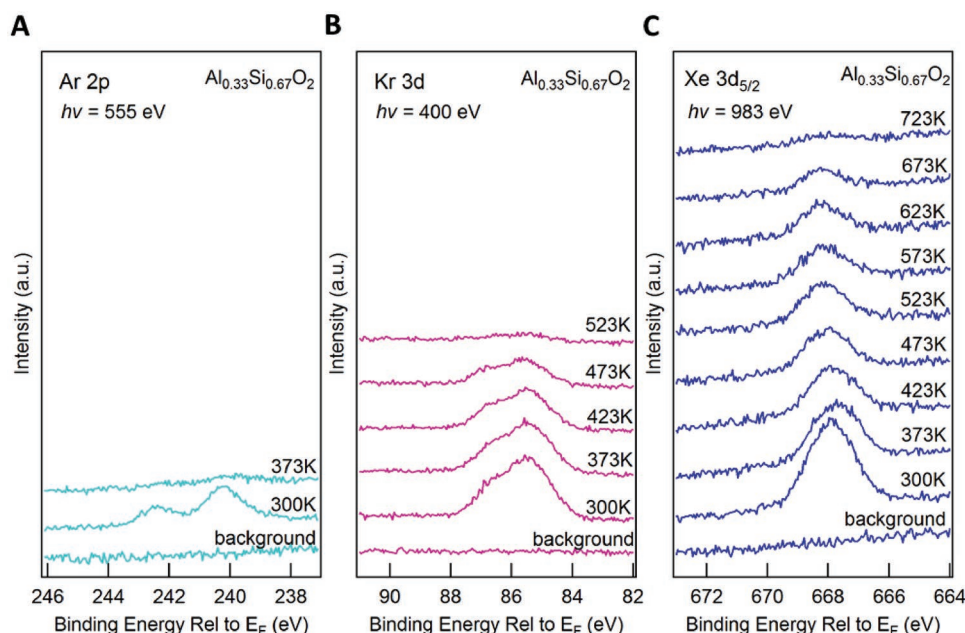


Figure 2. UHV XPS spectra of noble gas atoms [A] Ar 2p, B) Kr 3d_{5/2}, and C) Xe 3d_{5/2}] trapped in a aluminosilicate bilayer (Al_{0.33}Si_{0.67}O₂) as a function of temperature. The aluminosilicate was exposed to 2 mbar Ar, Kr or Xe for 10 minutes prior to evacuation and spectra acquisition.

which the E_{BE} for atoms trapped in the cages and at the interface are summarized in Table S1 (Supporting Information). Note that as part of the AP-XPS measurements, a fraction of the gas phase molecules can be ionized, which plays a crucial role in the trapping mechanism and will be discussed in detail in the following section. A rough estimation based the beam size, photon flux, gas pressure, photoionization cross section, and system geometry gives a rate of ion generation inside of the experimental chamber in the order of 10^{11} ions s^{-1} . However, only a small fraction of these ions is expected to reach the sample surface. The size of the nanocages in silica frameworks is ≈ 3.2 Å, defined by subtracting the vdW diameter of an O atom (≈ 3.0 Å) from the O–O distance (6.2 Å) at opposite sides of the middle layer of the nanocage.^[13b,18] Considering the vdW diameter of the noble gas atoms (i.e., He ≈ 2.80 Å, Ne ≈ 3.08 Å, Ar ≈ 3.76 Å, Kr ≈ 4.04 Å, Xe ≈ 4.32 Å, and Rn ≈ 4.40 Å),^[19] He and Ne atoms are too small to be trapped, while Ar, Kr, Xe, and Rn atoms have the right sizes (i.e., slightly larger than the cage) to remain in the nanocages at room temperature.

Aside from the silica bilayer, the aluminosilicate bilayer films also trap Ar, Kr, and Xe. XPS spectra of the trapped noble gas atoms in an aluminosilicate film (Al_{0.33}Si_{0.67}O₂) are plotted in Figure 2 at increasing temperatures. The aluminosilicate has stronger electrostatic interactions with the metal support, resulting in an interfacial space that is too small to trap noble gases.^[20] Therefore, the XPS peaks are assigned to noble gas atoms trapped in the nanocages of the aluminosilicate film. Desorption of these trapped noble gas atoms at 300 K is slow for Ar and negligible for Kr and Xe. For example, we showed in recent work that only 25% of trapped Ar atoms desorb in the ultrahigh vacuum (UHV) after 12 h.^[16] In the experiments reported here, there is virtually no desorption for trapped Kr and Xe atoms at room temperature. The air stability of the noble gas atoms in the nanocages was tested by taking a silica

bilayer sample with Xe trapped in it and exposing it to air for 4 h before putting it back into the experimental chamber. XPS spectra of the Xe 3d core level (Figure S3, Supporting Information) were taken before and after air exposure, showing that Xe atoms remain trapped.

The noble gas coverage Θ , defined as the number of trapped noble gas atoms per nanocage, is estimated by the ratio of the XPS peak areas between the Ar 2p, Kr 3d or Xe 3d, and Si 2p (Figure S4, Supporting Information), taking into account the photoionization cross sections for each core level at the used photon energy. The photon energies were chosen in order to have the same photoelectron kinetic energy, and thus the same electron transmission function, for all cases. The estimated saturation coverages are $\Theta_{sat} = 0.14 \pm 0.02$, 0.20 ± 0.02 , and 0.04 ± 0.02 for Ar, Kr, and Xe on the silica bilayer, respectively (Figure 5A–C). In the case of the aluminosilicate (Al_{0.33}Si_{0.67}O₂), these coverages are higher, i.e., 0.18 ± 0.02 (Ar), 0.26 ± 0.02 (Kr), and 0.12 ± 0.02 (Xe) (Figure 5D–F). A higher Θ_{sat} in aluminosilicates than silica can be attributed to their larger trapping energies as will be discussed in the following section. Note that vitreous regions are sometimes found on the surface in addition to the hexagonal prisms, especially for silica, and this may result in underestimating the coverage since the total density of hexagonal prism nanocages may be smaller than in the ideal crystalline structure.^[21]

DFT calculations are carried out to study the structures and energetics of noble gases (Ar, Kr, Xe, and Rn) trapping in both silica (SiO₂) and aluminosilicate (H_{0.125}Al_{0.375}Si_{0.625}O₂) frameworks. Silica films on $p(2 \times 1)$ -O/Ru(0001)^[22] and aluminosilicate films on Ru(0001) with $\Theta = 0.25$ and 0.5 are modeled. The structural changes of the frameworks upon noble gas trapping inside nanocages are quantified by monitoring changes in the film thickness and nanocage sizes in silica (Figure S5, Supporting Information) and aluminosilicate films (Figure S6,

Supporting Information). In order to characterize the structural deformation of the framework upon trapping the noble gases, we distinguish three different oxygen locations of the framework shown in the side view in Figure 1B in the direction normal to the surface: a) oxygen at the bottom (closest to ruthenium, O_b), b) oxygen in the middle (O_m), and c) oxygen at the top (furthest from ruthenium, O_t). The major changes are found in the O_m – O_m distances between oxygen atoms at opposite sides of the cage ($d(O_m$ – $O_m)$), due to the expansion of the nanocages. Taking $\Theta = 0.5$ as an example, $d(O_m$ – $O_m)$ increases by 0.05 Å (Ar), 0.08 Å (Kr), 0.14 Å (Xe), and 0.17 Å (Rn) in SiO_2 and 0.08 Å (Ar), 0.10 Å (Kr), 0.17 Å (Xe), and 0.20 Å (Rn) in $\text{H}_{0.125}\text{Al}_{0.375}\text{Si}_{0.625}\text{O}_2$. The distortion of the cages could potentially induce shifts in the vibrational phonon modes of the structure, as obtained by infrared reflection absorption spectroscopy (IRRAS). The most characteristic mode is associated with the vertical motion of the oxygen atoms linking the two layers in the bilayer structure, which for the case of SiO_2 is located at $\approx 1300\text{ cm}^{-1}$. Another phonon mode has been reported for this bilayer structure at $\approx 690\text{ cm}^{-1}$. However, our instrument has a lower wavelength cutoff at 800 cm^{-1} , rendering this lower-frequency mode inaccessible in our experiments. Previous work did not show any visible shift on the 1300 cm^{-1} mode upon Ar inclusion due to the negligible distortion of the bilayer upon Ar intake.^[16] Upon Xe trapping, however, there is an 8 cm^{-1} redshift in the signature interlayer phonon mode in IRRAS (Figure S7, Supporting Information), which could be explained by the distortion of the bilayer where $d(O_m$ – $O_m)$ increases by 0.14 Å and the film thickness ($d_z(O_t$ – $O_b)$) increases by 0.01 Å at $\Theta_{\text{Xe}} = 0.5$ (Figure S5D, Supporting Information). The redshift is accompanied by a large broadening of the phonon peak with the full width at half maximum changing from 10.2 to 14.4 cm^{-1} . This shift and broadening are reversible as Xe desorbs upon heating the sample to 873 K .

We calculated the adsorption energies (ΔE_{ads}) for gas atoms adsorbed outside the nanocage, $\Delta E_{\text{ads}} = E_{\text{sub+gas}^*} - (E_{\text{sub}} + E_{\text{gas}})$, where $E_{\text{sub+gas}^*}$, E_{sub} , and E_{gas} are the total energies for the adsorbed system (gas*–(alumino)silicate/O/Ru(0001)) and noninteracting individual components ((alumino)silicate/O/Ru(0001) and isolated gas atoms). Consistent with ΔE_{ads} in the order of $\approx 100\text{ meV}$ for noble gas atoms adsorbed on the Pd(111) surface,^[8] the calculated ΔE_{ads} is -0.16 eV (Ar), -0.19 eV (Kr), -0.24 eV (Xe), and -0.29 eV (Rn) for SiO_2 and -0.15 eV (Ar), -0.17 eV

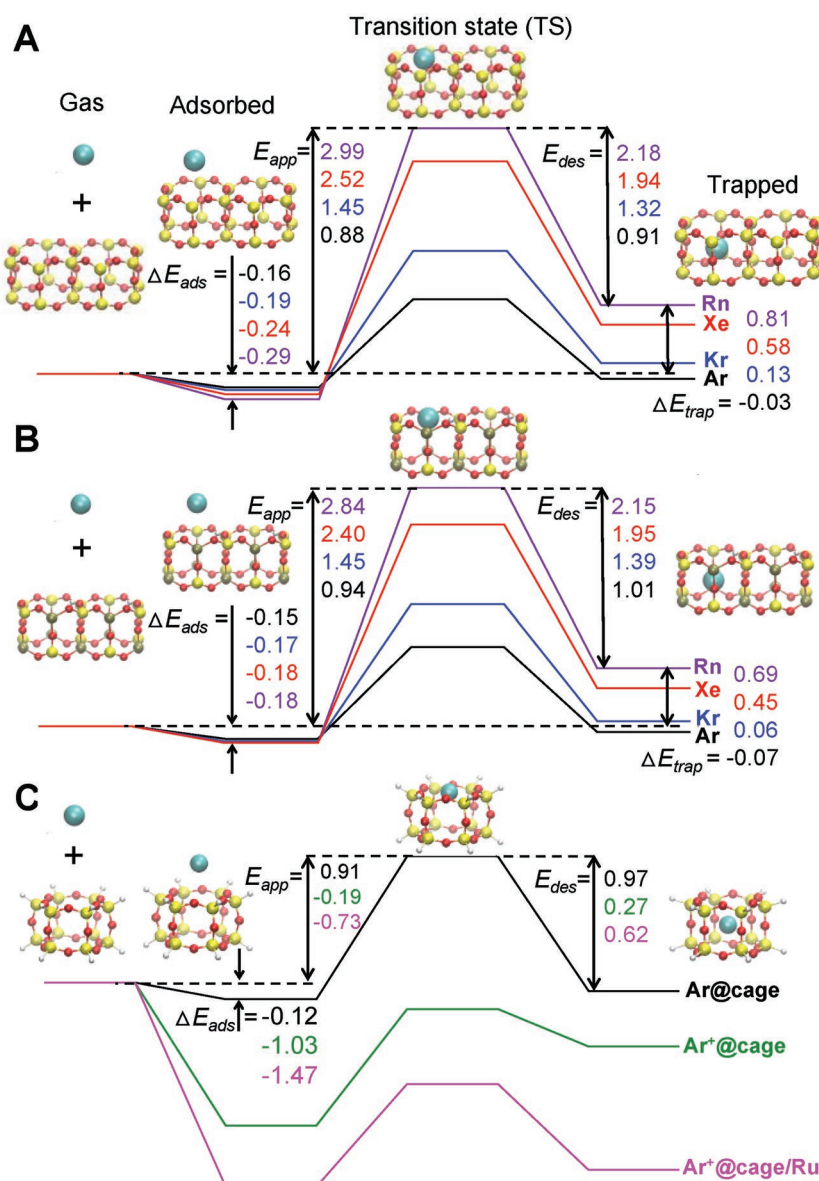


Figure 3. Potential energy diagram for the noble gas trapping. Potential energy diagram for Ar (black line), Kr (blue line), Xe (red line), and Rn (violet line) atoms being trapped in the A) silica and B) aluminosilicate bilayer film at $\Theta = 0.25$. Color code: Ar (black), Kr (blue), Xe (red), and Rn (violet). C) Potential energy diagram from constrained DFT calculations for a neutral Ar atom trapped inside a single freestanding silica nanocage terminated with H atoms (black line), Ar^+ trapped inside a single freestanding silica nanocage (green line), and Ar^+ trapping in a silica nanocage adsorbed on Ru surface (magenta line). Colors of energies correspond to colors of Ar@ cage (black), Ar^+ @ cage (green), and Ar^+ @ cage/Ru (magenta). ΔE_{ads} and ΔE_{trap} (in eV) represent the adsorption energy outside the nanocage and trapping energy inside the nanocage. E_{app} and E_{des} (in eV) represent the apparent trapping and desorption energy barriers.

(Kr), -0.18 eV (Xe), and -0.18 eV (Rn) for $\text{H}_{0.125}\text{Al}_{0.375}\text{Si}_{0.625}\text{O}_2$ (Figure 3). Due to the weak vdW interaction, noble gas atoms adsorbed outside the nanocages are not stable at noncryogenic conditions and can easily desorb at room temperature.

Noble gas atoms can be trapped inside the (alumino)silicate nanocage or at the silica/Ru(0001) interface. Trapping energies (ΔE_{trap}) are calculated from the relaxed structures of the (alumino)silicates before and after the noble gas trapping,

$\Delta E_{\text{trap}} = E_{\text{sub+gas(trap)}} - (E_{\text{sub}} + E_{\text{gas}})$, where $E_{\text{sub+gas(trap)}}$, E_{sub} , and E_{gas} are the total energies for (alumino)silicate/O/Ru(0001) with and without trapped gas, and isolated gas atoms, respectively. The calculated ΔE_{trap} are summarized in Figure 3 and Table S2 (Supporting Information), and the corresponding structures are summarized in Figures S5 and S6 (Supporting Information). For the noble gas atoms trapped in the nanocages at $\Theta = 0.25$, ΔE_{trap} is -0.03 eV (Ar), 0.13 eV (Kr), 0.58 eV (Xe), and 0.81 eV (Rn) for SiO_2 and -0.07 eV (Ar), 0.06 eV (Kr), 0.45 eV (Xe), and 0.69 eV (Rn) for $\text{H}_{0.125}\text{Al}_{0.375}\text{Si}_{0.625}\text{O}_2$. Unlike trapped Ar, significantly large positive trapping energies of Xe and Rn in both cases indicate that these trapped Xe and Rn are thermodynamically unstable, because the vdW diameters of Xe and Rn are >1 Å larger than the size of the nanocage, which also leads to larger trapping and desorption barriers than Ar and Kr.

Structures corresponding to noble gas atoms trapped at the silica/Ru(0001) interface are also studied. Compared to ΔE_{trap} of atoms in the nanocages, noble gas atoms trapped at the interface are energetically less favorable, which is partially due to the energy penalty associated with pushing the silica bilayer away from the substrate (Figure S8, Supporting Information). DFT results on the vertical displacement of the silica bilayer from the metallic support by CO molecules were also reported by Schlexer et al.^[23] Our results suggest that the nanocages in the (alumino)silicate frameworks are the preferred trapping sites over the interface, which is consistent with XPS results where the main peak is assigned to the noble gas atoms trapped in the nanocages.

2.2. Trapping Mechanism

The energetics of the noble gas trapping pathway is calculated from DFT using the climbing image nudged elastic band (CI-NEB) method^[24] for neutral noble gas atoms, including the initial state before adsorption, adsorbed states, transition states (TS), and trapped states. The minimum energy pathways are shown in Figure S9 (Supporting Information) for $\Theta = 0.25$ and $\Theta = 0.5$. In particular, we focus on the apparent activation energy barriers for noble gas trapping (E_{app}) and desorption (E_{des}), where E_{app} (E_{des}) is the energy difference between the transition state and the initial state before adsorption (the trapped state). In order to enter or escape from the nanocages, noble gases need to overcome these barriers, as shown in Figure 3A and Table S2 (Supporting Information). At the transition state, the nanocage in the silica framework expands substantially to allow noble gas atoms to enter. The calculated E_{app} (E_{des}) are 0.88 (0.91), 1.45 (1.32), 2.52 (1.94), and 2.99 (2.18) eV for Ar, Kr, Xe, and Rn trapped in the silica framework at $\Theta = 0.25$, respectively. Such high activation energies for trapping and desorption result mainly from the deformation energy of the hexagonal prisms at the transition state. As shown in Figure 3B, E_{des} (aluminosilicate) is larger than E_{des} (silica), which is consistent with a higher desorption temperature from the aluminosilicate film (Figure 5). The aluminosilicate film also has a smaller ΔE_{trap} (Figure 3B), which is related to a more stable trapped state. This can be understood as a result of longer Al–O bonds as compared to the Si–O bonds, which leads to

larger film thickness ($d_z(\text{O}_t\text{--O}_b)$) and less energetic penalty to distort O–Al–O angles as compared to O–Si–O angles.^[25] For example, $d(\text{O}_t\text{--O}_b)$ of the SiO_2 film is 4.26 Å, which increases to 4.51 Å in $\text{H}_{0.125}\text{Al}_{0.375}\text{Si}_{0.625}\text{O}_2$, creating a less confined space.

Strong evidence from both experiment and theory suggests that the ultrahigh E_{des} (about $1\text{--}2$ eV) is key to the noble gas atoms trapped in nanocages at noncryogenic temperatures. An intriguing question is how noble gas atoms overcome the large E_{app} (about $1\text{--}3$ eV) to enter the nanocages. Due to the presence of X-ray, it is highly possible that noble gas atoms are ionized in the gas phase. In the following, we first use DFT to investigate the energy pathway of rare gas ions trapping in 2D silica and show that noble gas cations experience significantly lower E_{app} than neutral atoms, which facilitates the trapping process. Then we provide experimental evidence to demonstrate that noble gas atoms are ionized by X-ray during the AP-XPS measurements before entering the nanocage.

There are two major factors that can influence the trapping of noble gas cations: electrostatic forces and Pauli repulsion. First, the electrostatic forces from the induced charges on the (alumino)silica bilayer and the image charges from the Ru substrate can pull the noble gas cation toward the nanocages, which effectively lowers E_{app} . Second, since a cation is smaller than the neutral atom, the energy cost of the cation to stretch the mouth of the cage in the transition state is lower than that of the neutral atom, due to a weaker Pauli repulsion. To provide a quantitative assessment, we calculated the energetics of Ar^+ trapping pathway in a silica nanocage using constrained DFT,^[26] where the silica bilayer is approximated by an isolated hexagonal nanocage terminated with H atoms and a positive charge is constrained on Ar^+ . This model naturally includes the effects of the polarization energy from the silica film and the Pauli repulsion between Ar^+ and the nanocage. The image potential of the Ru substrate is included separately using $U_{\text{im}} = -\frac{e^2}{16\pi\epsilon_0 |z - z_{\text{im}}|}$, where z is the atom position of the transition state and $z_{\text{im}} = 1.35$ Å is the image plane of the Ru.^[27]

As shown in Figure 3C, the minimum energy path for a neutral Ar atom (the black curve) to enter an isolated hexagonal nanocage is nearly the same as the extended bilayer system adsorbed on the Ru(0001) surface (Figure 3A), with a slightly larger E_{app} by 0.03 eV (Figure 3C). The green curve in Figure 3C represents the potential energy for Ar^+ trapping in a single silica cage from constrained DFT calculations. Compared with the $\Delta E_{\text{ads}} = -0.12$ eV of the neutral Ar in the adsorbed state outside the nanocage, ΔE_{ads} for Ar^+ is -1.03 eV, which is 0.91 eV lower in energy due to charge-induced charge attraction. After taking into account the polarization energy from the nanocage and smaller Ar^+ size, E_{app} of Ar^+ drops to -0.19 eV. Once the image potential is included (magenta curve in Figure 3C), E_{app} further drops to -0.73 eV. Overall, the ionization can lower E_{app} by 1.64 eV as compared to that of the neutral atom (0.91 eV) and makes the trapping of Ar^+ feasible at room temperature.

We note that if Ar^+ at the adsorbed state is neutralized by the silica/Ru heterojunction, E_{app} is restored to that of the neutral atom, unless Ar is ionized again. As shown in Figure S10A (Supporting Information), the Ar 3p state is located at ≈ 4 eV below the Fermi level (E_{F}) when Ar is adsorbed outside the nanocage. At the transition state, Ar 3p peak is broadened due to the

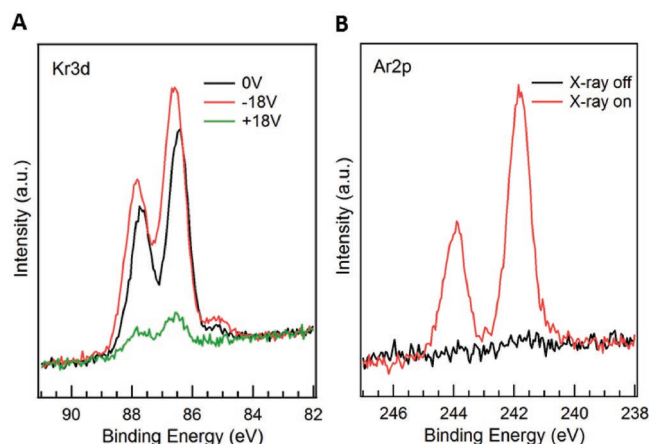


Figure 4. Sample bias-dependent noble gas trapping behavior proving the cationic nature of the noble gas species entering the nanocages. A) The silica bilayer was exposed to 2 mbar Kr for 10 min with 0 V (black), -18 V (red), and +18 V (green) sample bias, respectively, in the presence of an X-ray beam. The spectra were acquired under UHV conditions after evacuating the gas ($h\nu = 400$ eV). B) Effect of the X-ray beam on the ionization and trapping processes. The silica bilayer was exposed to 2 mbar Ar for 10 min in the presence (red) and absence (black) of an X-ray beam. The spectra were acquired under UHV conditions after evacuating the gas ($h\nu = 650$ eV).

hybridization with the nearby O atoms from the silica nanocage and the highest occupied molecular orbital (HOMO) of Ar is closer to E_F (Figure S10B, Supporting Information). Therefore, there is an increasing probability of the charge transfer from (alumino)silicate/Ru(1000) to Ar^+ through resonant tunneling as Ar^+ is pulling toward the nanocage by electrostatic forces.

In order to experimentally prove our hypothesis of the cationic nature of the noble gas species entering the nanocage, a silica bilayer was exposed to 2 mbar of Kr while biasing the sample to either attract the cations (-18 V) or repel them (+18 V). The results are shown in Figure 4A, where -18 V bias results in a slight increase in the coverage of Kr, while +18 V bias results in a drastic decrease of the population of trapped Kr. These results provide strong evidence supporting our model that the noble gas enters the nanocage in its cationic form. It is worth noting that, while in the case described above the noble gases are ionized by the synchrotron X-rays, no trapping is observed in a control experiment in the absence of X-rays (Figure 4B). The ionization could be achieved in many other less demanding methods without resort to X-rays, including, for example, subjecting the gas to a strong electric field.^[28] For example, the Xe trapping shown in Figure S3 (Supporting Information) was achieved by ionizing Xe by means of an electric field, using a sputter ion gun to generate ions without accelerating them toward the surface. Additionally, and intentionally, in that experiment the sample was not in line of sight with the sputter gun. Another relevant instance is nuclear power plants where gas atoms are inherently exposed to ionizing radiation.

2.3. Desorption Mechanism

Upon entering the cage, the cation is neutralized due to the electron transfer from the (alumino)silicate/Ru heterojunction. Even

in the case noble gas atom is ionized again on the now inside of the cage as part of the XPS measurement, typical lifetimes of the charged state are in the order of 10^{-15} s, much faster than the nuclear motion needed for desorption. Therefore, the atoms must desorb in the neutral state. The noble gas atoms at the interface are less stable than those in the nanocages and may desorb through the grain boundaries at low temperatures from silica, as described later in Figure 5. For example, from 298 to 373 K, the amount of trapped Kr decreases by 20% on the silica bilayer while there is almost no Kr desorption from the aluminosilicate bilayer, because there are no interfacial Ar, Kr, or Xe atoms at the aluminosilicate/Ru interface. The release temperature is defined as the temperature with the highest desorption rate (Table S3, Supporting Information), which is equivalent to the peak temperature in temperature programmed desorption (TPD) spectra. The release temperature from the silica framework for Ar, Kr, and Xe are 373, 473, and 623 K, respectively (Figure 5A–C). The desorption temperatures increase to 498 K for Kr and to 673 K for Xe in the aluminosilicate (Figure 5E,F). This report of Xe atoms trapped in the nanocages up to 673 K constitutes, to the best of our knowledge, the most stable case of noble gas atoms in confinement so far.^[29]

Since gas atoms are neutralized after entering the nanocages, it is important that we compare the E_{des} from DFT with that obtained from the desorption experiment (Figure 5). In order to obtain E_{des} from the experiment, the first-order reaction law $\Theta = \Theta_0 \exp(-kt)$ ^[30] was used, where Θ_0 was taken from the first XPS data point at 298 K. The desorption rate constants (k) were calculated using the Arrhenius equation $k = A \exp(-E_{\text{des}}/k_B T)$, where A , k_B , and T are the pre-exponential factor calculated from the transition state theory, the Boltzmann constant, and the temperature. In order to obtain good fittings for $\Theta(t, T)$, a distribution of E_{des} is expected, as labeled in Figure 5 (E_1 , E_2 , and E_3). Three E_{des} from the experiment with different coverage (Θ_{E1} , Θ_{E2} , and Θ_{E3}) could be rationalized by the fact that there are possible inhomogeneities in the ring size distributions during the film synthesis, especially for the (alumino)silicate, as reported by Lichtenstein et al.,^[21b,31] and distortions of the hexagonal prism cages.

The $\Theta(t, T)$ curves (red curve in Figure 5) with fitted E_{des} (E_1 , E_2 , E_3) agree well with the experiments under an assumption of the error bar from XPS (± 0.02 atoms per cage). The zero point energy (ZPE) corrected E_{des} ($E_{\text{des-DFT}}$ from Figure 5) is calculated to compare with the fitted E_{des} . The fitted E_{des} with the highest composition ratio agrees well with the $E_{\text{des-DFT}}$ considering a reasonable error bar of DFT energy barriers (± 0.1 eV),^[32] indicating that most of the noble gas atoms were trapped at the perfect hexagonal domains, and that it is the neutral gas atoms that desorb from the film. Take the desorption of Ar from a silica film as an example (Figure 5A). 44% of the Ar atoms are trapped in the hexagonal cages with the energy barrier $E_{\text{des}}(E_2) = 0.93$ eV, which agrees well with $E_{\text{des-DFT}} = 0.92$ eV from DFT calculations. E_1 and E_3 are within ± 0.1 from E_2 , likely corresponding to the Ar atoms trapped in other defect structures (e.g., distorted hexagonal prisms). The presence of the defect structures was observed in our previous work in the scanning tunneling microscopy (STM) images for the aluminosilicate film shown in Figure S11 (Supporting Information),^[25] where 45% of the hexagonal cages were surrounded by six-membered

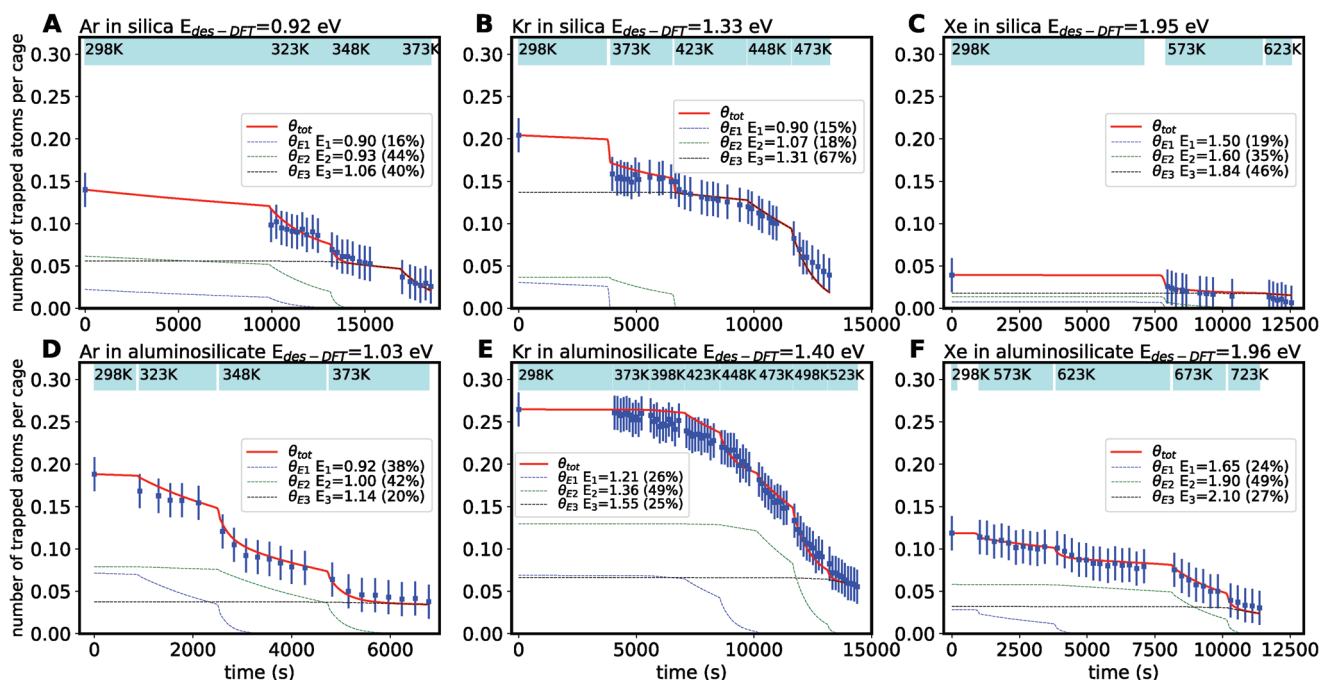


Figure 5. Desorption of trapped noble gases (Ar, Kr, and Xe) from 2D zeolite models. A–C) silica bilayer (SiO_2) and D–F) 2D aluminosilicate bilayer ($\text{Al}_{0.35}\text{Si}_{0.65}\text{O}_2$ in experiments and $\text{H}_{0.125}\text{Al}_{0.375}\text{Si}_{0.625}\text{O}_2$ in DFT). The number of trapped atoms per cage (Θ) is obtained from the normalized XPS peak areas (Ar 2p, Kr 3d, and Xe 3d) (blue dots). All XPS data are collected under UHV conditions after A,D) 2 mbar Ar, B,E) 2 mbar Kr, and C,F) 2 mbar Xe exposures. The error bars from XPS are ± 0.02 atoms per cage. The desorption curve (red curves) is fitted with three energy barriers, E_{des} (E_1 , E_2 , and E_3) by using the pre-exponential factors from transition state theory. Dotted blue, green, and black curves represent desorption Θ - t curves for gas trapped at the three fitted energy barriers. $E_{\text{des-DFT}}$ are DFT calculated desorption energy barriers with zero-point energy (ZPE) correction ($\Theta = 0.25$).

rings while 55% of the hexagonal cages were surrounded by non-six-membered rings. The non-six-membered rings induce distortions in the hexagonal prism cages, which would explain changes in the activation energy for the release. Defect structures were also predicted by calculations from other groups.^[33] It should be noted that in silica films (Figure 5A–C), the lowest fitted E_{des} (E_1) contribute to 16% (Ar), 15% (Kr), and 19% (Xe) of the trapped atoms, which are comparable to the proportion of the noble gas atoms trapped at the interface of silica/Ru(0001) (Figure S2, Supporting Information). Therefore, E_{des} (E_1) in Figure 5A–C is assigned to the interfacial trapped noble gas atoms that are likely to desorb through the grain boundaries, which also explains the drop of Θ at the initial heating stages as discussed above, which is observed in silica, but not in the aluminosilicates.

2.4. Separation of Noble Gases

The unprecedented ability to stabilize all noble gas atoms heavier than Ne makes these 2D materials not only an exciting new playground for fundamental studies of individual atoms in nanoconfinement, but also promising candidates for potential applications in noble gas storage and separation. We illustrate such potential by trapping a mixture of Ar, Kr, and Xe in the cages of a aluminosilicate film at room temperature and releasing them subsequently at higher temperatures. Here, the aluminosilicate bilayer ($\text{Al}_{0.35}\text{Si}_{0.65}\text{O}_2$) is exposed to 2 mbar of an equimolar noble gas mixture at 300 K for 20 min while

measuring XPS. Atoms of the three gases get simultaneously trapped in the cages as evident by XPS spectra taken after pumping out the gases. The sample is then heated while taking XPS spectra, and Figure 6 shows a plot of the Ar, Kr, and Xe content as a function of temperature. Kr atoms have the highest initial coverage (i.e., 0.06 per nanocage), consistent with higher coverage seen in the single-component noble gas trapping experiments discussed above. By increasing the temperature

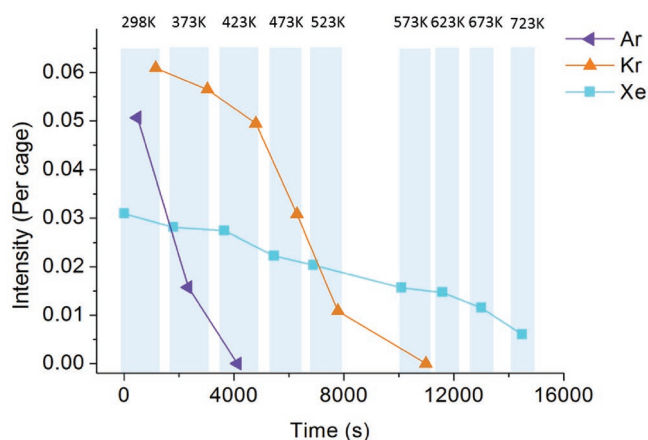


Figure 6. XPS analysis of mixed noble gas atoms trapped in a 2D aluminosilicate ($\text{Al}_{0.35}\text{Si}_{0.65}\text{O}_2$) bilayer. All XPS data are collected under UHV conditions after 2 mbar exposure to a mixture of noble gases ($n_{\text{Ar}}:n_{\text{Kr}}:n_{\text{Xe}} = 1:1:1$). The coverage (Θ) is calculated and displayed as a function of time and temperatures.

to 423 K, all trapped Ar atoms are released from the aluminosilicate bilayer, while Kr and Xe still have 81% and 89% left in the framework. These trapped Kr atoms can be completely removed from the film by further increasing the temperature to 573 K, where 51% of Xe atoms remain trapped in the framework. Simulated temperature programmed desorption curves for Ar, Kr, Xe, and Rn (Figure S12, Supporting Information) also illustrate the potential for separating different noble gases. Moreover, the 2D zeolite has a trapping capacity (9 wt% for Kr) comparable with other selective adsorbents like metal–organic frameworks (13 wt% for Kr).^[34] However, it should be noted that both the film quality and the ionization process are essential for such separations.

2.5. Other Important Implications

Our findings also provide important hints on the “missing” Xe problem,^[35] suggesting that the extremely low concentration of Xe in the atmosphere might result from Xe being trapped in, e.g., aluminosilicate minerals on the earth. An identical 2D aluminosilicate structure with hexagonal prism cages is also found in nature, as a multilayer material called hexacelsian,^[36] with barium ions separating the layers.^[37] Hexacelsian is thermodynamically very stable, and can also be synthesized by heating up Ba-exchanged Zeolite A, which is one of the most inexpensive zeolites, to high temperatures.^[38] The relatively low cost of producing synthetic hexacelsian opens the doors for exploring potential applications, including the trapping and separation of gases discussed above, ultrathin corrosion resistant coatings,^[13a,39] trapping of radioactive isotopes of noble gases, production of catalytically active 2D aluminosilicate nanosheets,^[10] and ultrathin membranes. The ability of these nanoporous 2D materials to host noble gas atoms (and potentially other species) in cages and at the interface with the metal support, also offer interesting possibilities for exploring nanoscale confinement effects in chemical reactions. This possibility is described in more detail in a recent topical review.^[40]

3. Conclusion

In summary, individual noble gas atoms (Ar, Kr, Xe, and Rn) can be trapped at 300 K in hexagonal prism nanocages (0.5 nm) of 2D silica and aluminosilicate by activated physisorption, while He and Ne are too small to remain in the cages. This opens up exciting opportunities for studying individual gas atoms under spatial confinement at high temperature with great detail, using extremely sensitive surface science techniques. Additionally, a variety of applications in gas capture and separation, with important implications in the environment and health, are envisioned. The trapping of noble gas atoms at noncryogenic temperature is detected in situ using XPS measurements and corroborated by DFT calculations. The noble gas atoms enter the cages as cations and become neutralized by the substrate after being trapped. We find that the larger the atom, the more stable it is in the cage, as evident by the higher desorption temperature and the higher activation energy for desorption. Furthermore, we demonstrate that a mixture of noble gases can be trapped and then separated,

taking advantage of their different desorption temperatures. The ionization-facilitated activated physisorption mechanism demonstrated in this study opens a new route to manipulate and engineer the molecule–surface interaction.

4. Experimental Section

Experimental methods: The Ru(0001) single crystal surface was cleaned with cycles of Ar⁺ sputtering and annealing at 1400 K. It was then exposed to 3×10^{-6} mbar O₂ at 1200 K in order to form a chemisorbed 3O-(2 × 2)-Ru(0001) overlayer. The silica and aluminosilicate bilayers were grown on the oxygen precovered ruthenium surface. Briefly, Si and Al were thermally evaporated onto the 3O-(2 × 2)-Ru(0001) surface at room temperature under 2×10^{-7} mbar of O₂, followed by oxidation at 1200 K in 3×10^{-6} mbar O₂ for 10 min and slowly cooled down in O₂ environment. Various 2D zeolite films were used in this work (SiO₂, Al_{0.33}Si_{0.67}O₂, and Al_{0.35}Si_{0.65}O₂). The relative aluminum content was determined by comparing the XPS peak intensities of the Al 2s and Si 2p. In DFT calculation, HAl_{0.375}Si_{0.625}O₂ was used to model the aluminosilicate films.

AP-XPS measurements were carried out at the 23-ID-2 beamline (IOS) of the National Synchrotron Light Source II (NSLS-II) and the X1A1 beamline of NSLS. The main chamber (base pressure = 2×10^{-9} mbar) of the end station was equipped with a differentially pumped hemispherical analyzer (Specs Phoibos 150 NAP), which was offset by 70° from the incident synchrotron light. IRRAS measurements were carried out using a home-built system described previously.^[41] The noble gases (He, Ne, Ar, Kr, and Xe) were introduced into the main chamber through precision variable leak valves for the trapping studies.

Computational Methods: DFT calculations were performed using plane-wave basis set and the projector augmented wave formalism implemented in the Vienna Ab initio simulation package (VASP).^[42] The consistent exchange van der Waals density functional (vdW-DF-cx)^[43] was used to describe the nonlocal vdW interactions. The choice of vdW-DF-cx was justified by its good performance for both Ru and chabazite, as tested in the previous works.^[13b,44] Ru(0001) substrate was modeled using five layers of Ru atoms and chemisorbed O atoms with a 0.5 ML coverage ($p(2 \times 1)$ -O/Ru(0001)). The system consists of silicate bilayer films on $p(2 \times 1)$ -O/Ru(0001) with two noble gas trapping concentrations. The lower concentration consists of gas-(SiO₂)₁₆/8O/Ru(0001) in a 10.784 Å × 9.339 Å × 27 Å super cell where 25% of the cages are filled with gas atoms ($\Theta = 0.25$) while a higher concentration with gas-(SiO₂)₈/4O/Ru(0001) in a 5.392 Å × 9.339 Å × 27 Å super cell where 50% of the cages are filled ($\Theta = 0.5$). A kinetic energy cutoff of 800 eV was used, and the Brillouin zone was sampled with $8 \times 4 \times 1$ for $\Theta = 0.5$ and $4 \times 4 \times 1$ for $\Theta = 0.25$. Silicate films with noble gas atoms, chemisorbed O atoms, and top two layers of Ru atoms were allowed to relax in the structural optimization until forces are smaller than 0.01 eV Å⁻¹. The core-level binding energies (E_{BE}) were calculated using the transition state model.^[45] The results were extrapolated to the infinite supercell size limit as described in the previous work.^[13b] All E_{BE} values of Ar 2p, Kr 3d, and Xe 3d were given relative to the E_{BE} of trapped atoms at the interface (Table S1, Supporting Information). The static dielectric constant of the silica film was calculated using VASP. The ionic contribution to the dielectric constant was calculated by the perturbation theory as implemented in VASP. Constrained DFT calculations were performed with the cc-pvtz basis set^[46] using Q-chem.^[47]

In order to obtain E_{des} from the $\Theta(t, T)$ data from experiment, the first-order reaction law $\Theta = \Theta_0 \exp(-kt)$ ^[30] was used, where Θ_0 were taken from the first XPS data point from 298 K. The desorption rate constants (k) were evaluated based on the Arrhenius equation $k = A \exp(-E_{des}/k_B T)$ ^[48] where k_B is the Boltzmann constant and T is the temperature in desorption experiments. $\Theta(t, T)$ was then fitted with the experiment data to obtain the desorption barriers E_{des} . Three E_{des} are needed due to the defects. The fitted E_{des} were then compared with $E_{des-DFT}$ from DFT calculated using the climbing image nudged elastic

band method (CI-NEB)^[24] implemented in VASP. To compare with E_{des} from the experiment, E_{des} in $\Theta = 0.25$ were used and ZPE correction^[32a] were included. The ZPE corrected E_{des} are summarized in Table S2 (Supporting Information). The pre-exponential factor A is calculated based on the transition state theory $A = \frac{1}{L} \sqrt{\frac{k_B T}{2\pi m}} \exp\left(\frac{\Delta S}{k_B}\right)$,^[49] where L is the thickness of the bilayer after the trapping of atoms and m is the mass of the trapped atoms. ΔS is the entropy difference of the initial (S_{ini}) and the transition state (S_{ts}). In canonical ensemble, the entropy is calculated as $S = k_B \sum_0^n \left[\frac{x_i}{e^{x_i} - 1} - \ln(1 - e^{-x_i}) \right]$, where $x_i = \frac{h\nu_i}{k_B T}$, and n is the number of phonon modes.^[50] The vibrational frequencies were calculated by the finite displacement method as implemented in VASP. ΔS are summarized in Table S2 (Supporting Information). During the calculations of the vibrational frequencies, the positions of the bilayer and Ru substrate are kept fixed.

Supporting Information

Supporting Information is available from the Wiley Online Library or from the author.

Acknowledgements

J.-Q.Z. and M.W. contributed equally to this work. Research was carried out at the Center for Functional Nanomaterials and the Scientific Data and Computing Center, a component of the Computational Science Initiative and the 23-ID-2 (IOS) beamline of the National Synchrotron Light Source II, Brookhaven National Laboratory, which are supported by the U.S. Department of Energy, Office of Basic Energy Sciences, under Contract No. DE-SC0012704. This research used resources of the National Energy Research Scientific Computing Center, a DOE Office of Science User Facility supported by the Office of Science of the U.S. Department of Energy under Contract No. DE-AC02-05CH11231. J.-Q.Z. and M.W. were supported by BNL LDRD Project No. 15-010. J.-Q.Z. and J.A.B. were the main experimenters. M.W., Q.W., and D.L. carried out the DFT calculations. J.-Q.Z. and M.W. wrote the manuscript. N.A., J.D.K., T.N., and A.M.B. participated in the experiments. All authors participated in discussions, data analysis, and manuscript preparation. J.A.B. and D.L. supervised the experimental and theoretical work, respectively.

Conflict of Interest

The authors declare no conflict of interest.

Keywords

2D zeolites, activated physisorption, gas separation, noble gas clathrate, single atom trapping

Received: September 18, 2018

Revised: January 29, 2019

Published online: March 6, 2019

[1] F. G. Kerry, *Industrial Gas Handbook: Gas Separation and Purification*, CRC Press, Boca Raton, FL **2007**.

[2] a) N. R. Soelberg, T. G. Garn, M. R. Greenhalgh, J. D. Law, R. Jubin, D. M. Strachan, P. K. Thallapally, *Sci. Technol. Nucl. Install.* **2013**, 2013, 1; b) R. Jubin, *Summary of FY-12 Off-Gas Sigma Team Activities*, Oak Ridge National Laboratory, Oak Ridge, TN **2012**.

- [3] <https://www.epa.gov/radon/health-risk-radon>.
- [4] S. Kawai, A. S. Foster, T. Björkman, S. Nowakowska, J. Björk, F. F. Canova, L. H. Gade, T. A. Jung, E. Meyer, *Nat. Commun.* **2016**, 7, 11559.
- [5] H. Dil, J. Lobo-Checa, R. Laskowski, P. Blaha, S. Berner, J. Osterwalder, T. Greber, *Science* **2008**, 319, 1824.
- [6] a) R. Larciprete, S. Colonna, F. Ronci, R. Flammini, P. Lacovig, N. Apostol, A. Politano, P. Feulner, D. Menzel, S. Lizzit, *Nano Lett.* **2016**, 16, 1808; b) C. Herbig, E. H. Åhlgren, U. A. Schröder, A. J. Martínez-Galera, M. A. Arman, J. Kotakoski, J. Knudsen, A. V. Krasheninnikov, T. Michely, *Phys. Rev. B* **2015**, 92, 085429.
- [7] R. Vanselow, R. F. Howe, *Chemistry and Physics of Solid Surfaces VII*, Vol. 10, Springer Science & Business Media, Berlin **2012**.
- [8] J. L. Da Silva, C. Stampfl, *Phys. Rev. B* **2008**, 77, 045401.
- [9] a) C. Büchner, L. Lichtenstein, X. Yu, J. A. Boscoboinik, B. Yang, W. E. Kaden, M. Heyde, S. K. Shaikhutdinov, R. Włodarczyk, M. Sierka, J. Sauer, H.-J. Freund, *Chem. - Eur. J.* **2014**, 20, 9176; b) J. A. Boscoboinik, X. Yu, B. Yang, F. D. Fischer, R. Włodarczyk, M. Sierka, S. Shaikhutdinov, J. Sauer, H.-J. Freund, *Angew. Chem., Int. Ed.* **2012**, 51, 6005.
- [10] J. A. Boscoboinik, X. Yu, E. Emmez, B. Yang, S. Shaikhutdinov, F. D. Fischer, J. Sauer, H.-J. Freund, *J. Phys. Chem. C* **2013**, 117, 13547.
- [11] J. A. Boscoboinik, S. Shaikhutdinov, *Catal. Lett.* **2014**, 144, 1987.
- [12] S. Kulprathipanja, *Zeolites in Industrial Separation and Catalysis*, John Wiley & Sons, Inc., Weinheim **2010**.
- [13] a) J.-Q. Zhong, J. Kestell, I. Waluyo, S. Wilkins, C. Mazzoli, A. Barbour, K. Kaznatcheev, M. Shete, M. Tsapatsis, J. A. Boscoboinik, *J. Phys. Chem. C* **2016**, 120, 8240; b) M. Wang, J.-Q. Zhong, J. Kestell, I. Waluyo, D. J. Stacchiola, J. A. Boscoboinik, D. Lu, *Top. Catal.* **2017**, 60, 481.
- [14] a) E. I. Altman, J. Götz, N. Samudrala, U. D. Schwarz, *J. Phys. Chem. C* **2013**, 117, 26144; b) J.-H. Jhang, C. Zhou, O. E. Dagdeviren, G. S. Hutchings, U. D. Schwarz, E. I. Altman, *Phys. Chem. Chem. Phys.* **2017**, 19, 14001; c) G. S. Hutchings, J.-H. Jhang, C. Zhou, D. Hynek, U. D. Schwarz, E. I. Altman, *ACS Appl. Mater. Interfaces* **2017**, 9, 11266; d) X. Yu, B. Yang, J. A. Boscoboinik, S. Shaikhutdinov, H.-J. Freund, *Appl. Phys. Lett.* **2012**, 100, 151608.
- [15] C. R. M. Jackson, S. W. Parman, S. P. Kelley, R. F. Cooper, *Nat. Geosci.* **2013**, 6, 562.
- [16] J.-Q. Zhong, M. Wang, N. Akter, J. D. Kestell, A. M. Boscoboinik, T. Kim, D. J. Stacchiola, D. Lu, J. A. Boscoboinik, *Nat. Commun.* **2017**, 8, 16118.
- [17] B. Yao, S. Mandra, J. O. Curry, S. Shaikhutdinov, H.-J. Freund, J. Schrier, *ACS Appl. Mater. Interfaces* **2017**, 9, 43061.
- [18] D. Löffler, J. J. Uhlich, M. Baron, B. Yang, X. Yu, L. Lichtenstein, L. Heinke, C. Büchner, M. Heyde, S. Shaikhutdinov, H. J. Freund, R. Włodarczyk, M. Sierka, J. Sauer, *Phys. Rev. Lett.* **2010**, 105, 146104.
- [19] M. Mantina, A. C. Chamberlin, R. Valero, C. J. Cramer, D. G. Truhlar, *J. Phys. Chem. A* **2009**, 113, 5806.
- [20] M. Wang, J.-Q. Zhong, D. J. Stacchiola, J. A. Boscoboinik, D. Lu, *J. Phys. Chem. C* **2018**, <https://doi.org/10.1021/acs.jpcc.8b05853>.
- [21] a) B. Yang, W. E. Kaden, X. Yu, J. A. Boscoboinik, Y. Martynova, L. Lichtenstein, M. Heyde, M. Sterrer, R. Włodarczyk, M. Sierka, J. Sauer, S. Shaikhutdinov, H.-J. Freund, *Phys. Chem. Chem. Phys.* **2012**, 14, 11344; b) L. Lichtenstein, M. Heyde, H.-J. Freund, *J. Phys. Chem. C* **2012**, 116, 20426.
- [22] H. Pfnür, G. Held, M. Lindroos, D. Menzel, *Surf. Sci.* **1989**, 220, 43.
- [23] P. Schlexer, G. Pacchioni, R. Włodarczyk, J. Sauer, *Surf. Sci.* **2016**, 648, 2.
- [24] G. Henkelman, B. P. Uberuaga, H. Jónsson, *J. Chem. Phys.* **2000**, 113, 9901.
- [25] J. A. Boscoboinik, X. Yu, B. Yang, S. Shaikhutdinov, H.-J. Freund, *Microporous Mesoporous Mater.* **2013**, 165, 158.

- [26] a) P. Dederichs, S. Blügel, R. Zeller, H. Akai, *Phys. Rev. Lett.* **1984**, 53, 2512; b) Q. Wu, T. Van Voorhis, *Phys. Rev. A* **2005**, 72, 024502; c) Q. Wu, C.-L. Cheng, T. Van Voorhis, *J. Chem. Phys.* **2007**, 127, 164119.
- [27] W. Berthold, U. Höfer, P. Feulner, D. Menzel, *Chem. Phys.* **2000**, 251, 123.
- [28] X. Lu, G. V. Naidis, M. Laroussi, K. Ostrikov, *Phys. Rep.* **2014**, 540, 123.
- [29] A. I. Joseph, S. H. Lapidus, C. M. Kane, K. T. Holman, *Angew. Chem., Int. Ed.* **2015**, 54, 1471.
- [30] A. D. McNaught, A. D. McNaught, *Compendium of Chemical Terminology*, Vol. 1669, Blackwell Science, Oxford **1997**.
- [31] L. Lichtenstein, C. Büchner, B. Yang, S. Shaikhutdinov, M. Heyde, M. Sierka, R. Włodarczyk, J. Sauer, H.-J. Freund, *Angew. Chem., Int. Ed.* **2012**, 51, 404.
- [32] a) K. Honkala, A. Hellman, I. Remediakis, A. Logadottir, A. Carlsson, S. Dahl, C. H. Christensen, J. K. Nørskov, *Science* **2005**, 307, 555; b) S. Gudmundsdóttir, E. Skúlason, K.-J. Weststrate, L. Juurlink, H. Jónsson, *Phys. Chem. Chem. Phys.* **2013**, 15, 6323.
- [33] T. Björkman, S. Kurasch, O. Lehtinen, J. Kotakoski, O. V. Yazyev, A. Srivastava, V. Skakalova, J. H. Smet, U. Kaiser, A. V. Krasheninnikov, *Sci. Rep.* **2013**, 3, 3482.
- [34] L. Chen, P. S. Reiss, S. Y. Chong, D. Holden, K. E. Jelfs, T. Hasell, M. A. Little, A. Kewley, M. E. Briggs, A. Stephenson, K. M. Thomas, J. A. Armstrong, J. Bell, J. Busto, R. Noel, J. Liu, D. M. Strachan, P. K. Thallapally, A. I. Cooper, *Nat. Mater.* **2014**, 13, 954.
- [35] a) C. Sanloup, B. C. Schmidt, E. M. C. Perez, A. Jambon, E. Gregoryanz, M. Mezouar, *Science* **2005**, 310, 1174; b) Q. Zhu, D. Y. Jung, A. R. Oganov, C. W. Glass, C. Gatti, A. O. Lyakhov, *Nat. Chem.* **2013**, 5, 61; c) L. Zhu, H. Liu, C. J. Pickard, G. Zou, Y. Ma, *Nat. Chem.* **2014**, 6, 644.
- [36] I. O. Galuskina, E. V. Galuskin, K. Prusik, Y. Vapnik, P. Dzierżanowski, M. Murashko, *Mineral. Mag.* **2015**, 79, 1229.
- [37] B. Yoshiki, K. Matsumoto, *J. Am. Ceram. Soc.* **1951**, 34, 283.
- [38] a) J. Djordjevic, V. Dondur, R. Dimitrijevic, A. Kremenovic, *Phys. Chem. Chem. Phys.* **2001**, 3, 1560; b) R.-D. Penzhorn, P. Schuster, H. Leitzig, H. E. Noppel, *Ber. Bunsenges. Phys. Chem.* **1982**, 86, 1077.
- [39] E. Emmez, J. A. Boscoboinik, S. Tenney, P. Sutter, S. Shaikhutdinov, H.-J. Freund, *Surf. Sci.* **2016**, 646, 19.
- [40] J. A. Boscoboinik, *J. Phys.: Condens. Matter* **2019**, 31, 063001.
- [41] J. D. Kestell, K. Mudiyanse, X. Ye, C.-Y. Nam, D. Stacchiola, J. Sadowski, J. A. Boscoboinik, *Rev. Sci. Instrum.* **2017**, 88, 105109.
- [42] a) G. Kresse, J. Furthmüller, *Phys. Rev. B* **1996**, 54, 11169; b) G. Kresse, J. Furthmüller, *Comput. Mater. Sci.* **1996**, 6, 15.
- [43] a) T. Björkman, *J. Chem. Phys.* **2014**, 141, 074708; b) K. Berland, P. Hyldgaard, *Phys. Rev. B* **2014**, 89, 035412.
- [44] N. Akter, M. Wang, J.-Q. Zhong, Z. Liu, T. Kim, D. Lu, J. A. Boscoboinik, D. J. Stacchiola, *Top. Catal.* **2018**, 61, 419.
- [45] C. Göransson, W. Olovsson, I. A. Abrikosov, *Phys. Rev. B* **2005**, 72, 134203.
- [46] T. H. Dunning Jr., *J. Chem. Phys.* **1989**, 90, 1007.
- [47] Y. Shao, Z. Gan, E. Epifanovsky, A. T. Gilbert, M. Wormit, J. Kussmann, A. W. Lange, A. Behn, J. Deng, X. Feng, *Mol. Phys.* **2015**, 113, 184.
- [48] K. A. Connors, *Chemical Kinetics: the Study of Reaction Rates in Solution*, John Wiley & Sons, Inc., Weinheim **1990**.
- [49] a) D. Chandler, *J. Chem. Phys.* **1978**, 68, 2959; b) Z. Yuan, A. Govind Rajan, R. P. Misra, L. W. Drahushuk, K. V. Agrawal, M. S. Strano, D. Blankschtein, *ACS Nano* **2017**, 11, 7974.
- [50] A. A. Gokhale, S. Kandoi, J. P. Greeley, M. Mavrikakis, J. A. Dumesic, *Chem. Eng. Sci.* **2004**, 59, 4679.